ISSN 1027-4510, Journal of Surface Investigation. X-ray, Synchrotron and Neutron Techniques, 2007, Vol. 1, No. 6, pp. 630–636. © Pleiades Publishing, Ltd., 2007.
Original Russian Text © R.V. Lapshin, 2007, published in Poverkhnost'. Rentgenovskie, Sinkhrotronnye i Neitronnye Issledovaniya, No. 11, pp. 13–20.

A Method for Automatic Correction of Drift-Distorted SPM Images

R. V. Lapshin

Lukin State Research Institute for Problems in Physics, Zelenograd, Moscow, 124460 Russia

Received September 25, 2006

Abstract—A method for automatic correction of drift-distorted surface images obtained using a scanning probe microscope is developed. For the case of slowly varying drifts, simple linear transformations describing the observed distortions are constructed. One or two pairs of counter-scanned images (CSIs) are used as initial data. A system of linear equations is solved by finding the coordinate of the same surface feature in each CSI. The solutions obtained, i.e., linear transformation coefficients, are used to correct drift-induced distortions in horizontal and vertical planes. Two nonlinear drift correction methods are proposed, which provide a better accuracy in comparison with the linear correction method. The developed method can be used in feature-oriented scanning of the surface.

DOI: 10.1134/S102745100706002X

INTRODUCTION

The measurement accuracy of the surface relief with physical sizes of elements from several angströms to several tens of nanometers is determined in many respects by the drift of the scanning probe microscope (SPM). As a rule, the instrument drift includes two main components: a thermal component associated with thermal deformation of mechanical units and a component caused by creep of the piezoelectric manipulators used [1]. The drift can be suppressed by active compensation during measurement [2] and/or correction of the results of scanning after measurement [3–6].

The attraction of image-correcting methods (in comparison with compensating techniques), among which is the method [7] proposed in this paper, is that distortions can be corrected without modernizing the microscope itself. Moreover, unlike passive methods, active drift compensation introduces additional noises, which does not allow its use for measurements at the microscope resolution limit.

DESCRIPTION OF THE METHOD

An analysis of distortions caused by microscope probe drift with respect to the sample surface shows that the drift results in stretching/compression of the image along the x and y raster axes in the lateral plane and image skew due to shifts of image lines/columns with respect to each other. The same, but with respect to the relief height, occurs in the vertical plane, where the differences in heights are incorrectly imaged and an additional nonexistent surface slope appears.

Assuming that the drift rate during scanning of small images varies slowly [7, 8], these distortions can be written as the following linear transformations:

$$\begin{aligned}\bar{x}(x, y) &= x + (K_x - 1)\{x + [(k+1)m_x + 1]y\},\\ \bar{y}(x, y) &= y + (K_y - 1)\{x + [(k+1)m_x + 1]y\},\\ \bar{z}(x, y) &= z(x, y) - (K_z - 1)\{x + [(k+1)m_x + 1]y\},\end{aligned} \quad (1)$$

where $\bar{x}$, $\bar{y}$, $\bar{z}$ are the coordinates of points of the corrected image; x, y, z are the coordinates of points of the drift-distorted image; K_x, K_y, K_z are the linear transformation coefficients (LTCs); k is the ratio of the probe velocity v_x in the line in the forward trace to that in the backward trace; and m_x is the number of points (without unity) in the line of the distorted image, which defines the range of variable $x = 0, \ldots, m_x$. To find unknown LTCs K_x, K_y, K_z, the surface is counter-scanned, which yields one or two image pairs. Their lines are drawn in opposite directions, and shifts from line to line in one image are performed in the direction opposite to the shift direction in another image. Image scanning speeds are set equal. In what follows, these images will be referred to as counter-scanned images (CSIs).

A characteristic of CSIs is the existence of a common point for both images, which we will call the coincidence point (CP). At this point, the sweep path of the first forward image comes to an end, while the sweep path of the second counter image begins.

If there is the same surface feature in each image of the obtained pair, having determined its lateral coordinates (x_1, y_1) and (x_2, y_2), we can write the following system of equations:

$$\begin{aligned}\bar{x}_1(m_x - x_1, m_y - y_1) &= \bar{x}_2(x_2, y_2),\\ \bar{y}_1(m_x - x_1, m_y - y_1) &= \bar{y}_2(x_2, y_2),\end{aligned} \tag{2}$$

where m_y is the number of points (without unity) in the column of the distorted image, which defines the range of variable $y = 0, ..., m_y$.

In general, to correct drift-induced distortions, it is sufficient to detect only one feature in the CSI and to determine its lateral coordinates. Practical SPM images have a finite resolution, are noisy, and contain failure regions; therefore, to more accurately determine correction parameters, it is desirable to use all surface features, except for those at image edges, where strong nonlinear distortions are possible [9, 10].

Thus, with the entirety of all detected features represented by its center of mass with the coordinates (x_1, y_1) and (x_2, y_2) in the corresponding CSI, and with account taken of transformations (1), Eqs. (2) can be rewritten as

$$\begin{aligned}m_x - x_1 + (K1_x - 1)\{m_x - x_1 + [(k+1)m_x + 1]\\ \times (m_y - y_1)\} = x_2 + (K2_x - 1)\\ \times \{x_2 + [(k+1)m_x + 1]y_2\},\\ m_y - y_1 + (K1_y - 1)\{m_x - x_1 + [(k+1)m_x + 1]\\ \times (m_y - y_1)\} = y_2 + (K2_y - 1)\\ \times \{x_2 + [(k+1)m_x + 1]y_2\}.\end{aligned} \tag{3}$$

The relation between coefficients *K1* and *K2* in CSIs is very simple,

$$\begin{aligned}K2_x &= 2 - K1_x,\\ K2_y &= 2 - K1_y,\\ K2_z &= 2 - K1_z.\end{aligned} \tag{4}$$

Substituting the coefficients $K2_x$ and $K2_y$ from formulas (4) into Eqs. (3), we find the sought-for LTCs $K1_x$ and $K1_y$ of the first image,

$$\begin{aligned}K1_x &= \frac{x_1 + x_2 - m_x}{x_2 - x_1 + m_x + [(k+1)m_x + 1](y_2 - y_1 + m_y)} + 1,\\ K1_y &= \frac{y_1 + y_2 - m_y}{x_2 - x_1 + m_x + [(k+1)m_x + 1](y_2 - y_1 + m_y)} + 1,\end{aligned} \tag{5}$$

knowing which and using relations (4), we determine the LTCs $K2_x$ and $K2_y$ of the second image. Then, using the obtained coefficients and transformations (1), we correct CSIs 1 and 2 in the lateral plane.

For the points of the CSI overlap area, which are corrected in the lateral plane, the following equation can be written:

$$\bar{z}_1(\bar{x}, \bar{y}) = \bar{z}_2(\bar{x}, \bar{y}). \tag{6}$$

The transformations in the lateral plane, which are inverse to transformations (1), are as follows:

$$\begin{aligned}x(\bar{x}, \bar{y}) &= \frac{\{(K_y - 1)[(k+1)m_x + 1] + 1\}\bar{x} - (K_x - 1)[(k+1)m_x + 1]\bar{y}}{K_x + (K_y - 1)[(k+1)m_x + 1]},\\ y(\bar{x}, \bar{y}) &= \frac{(1 - K_y)\bar{x} + K_x\bar{y}}{K_x + (K_y - 1)[(k+1)m_x + 1]}.\end{aligned} \tag{7}$$

Using the identity $\bar{z}(x, y) \equiv \bar{z}(\bar{x}, \bar{y})$, in which the coordinates $\bar{x}$, $\bar{y}$ of the overlap area are related to the coordinates x, y of the rectangular raster of the corresponding CSI through transformations (7), and using the expression for $\bar{z}$ in system (1), Eq. (6) can be written in the expanded form as

$$\begin{aligned}z_1(m_x - x_1, m_y - y_1) - (K1_z - 1)\{m_x - x_1\\ + [(k+1)m_x + 1](m_y - y_1)\}\\ = z_2(x_2, y_2) + (K2_z - 1)\{x_2 + [(k+1)m_x + 1]y_2\}\\ - (K1_z - 1)\{m_x + [(k+1)m_x + 1]m_y\}.\end{aligned} \tag{8}$$

From Eq. (8), using relation (4) between the coefficients $K1_z$ and $K2_z$, it is easy to express the coefficient $K1_z$ as

$$K1_z = \frac{z_2(x_2, y_2) - z_1(m_x - x_1, m_y - y_1)}{x_1 + x_2 + [(k+1)m_x + 1](y_1 + y_2)} + 1, \tag{9}$$

which is calculated for all points $(\bar{x}, \bar{y})$ of the overlap area and is then averaged. Knowing the coefficient K_z, we correct each image in the vertical plane according to the expression for $\bar{z}$ in transformations (1).

Finally, we bring the obtained images into coincidence at the CP and average the relief in the overlap area. In such a way, we obtain the corrected surface image with eliminated distortions caused by the x, y, and z drifts and a decreased noise level.

The corrected images of the first and second CSI pairs are brought into coincidence by making coincident the corrected centroid positions of sets of features common for all four images, followed by averaging the relief in the overlap area.

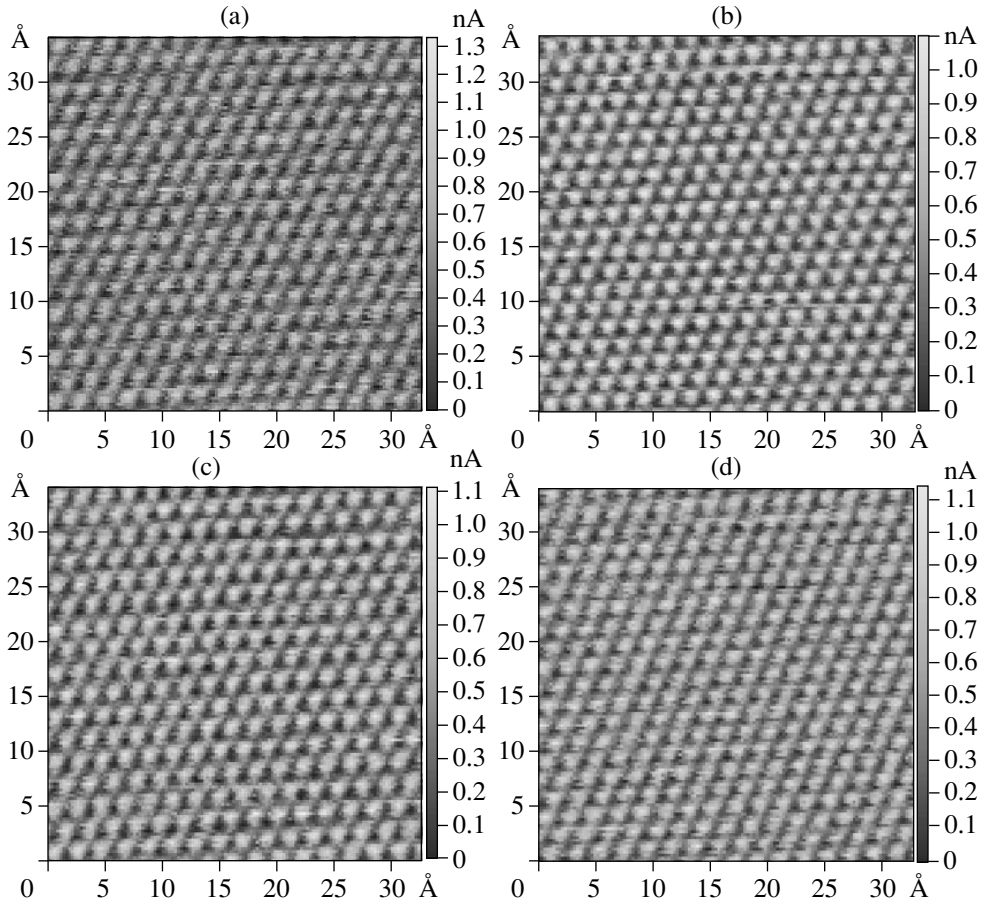

Fig. 1. Drift-distorted CSIs of the atomic surface of pyrolytic graphite: (a, b) the first CSI pair and (c, d) the second CSI pair. Measurement mode: STM, constant height, $U_{tun} = 85$ mV, and $I_{tun} = 750$ pA. The number of raster points is $m_x = m_y = 127$. The scanning step is $\Delta_x = 0.257$ Å and $\Delta_y = 0.269$ Å. The number of averagings at the raster point is 15. The scanning speed is $v_x = 187.6$ Å/s ($k = 1$). The scanning time is 1 min 29 s. The average magnitude of the drift velocity in the lateral plane is 0.1 Å/s. The maximum drift-induced relative errors of measurements in the lateral plane are (a, b) 7.8% and (c, d) 8.0%.

The search for features in the CSI and the determination of their lateral coordinates can be performed manually; however, the use of the recognition procedure [8, 11] allows full automation of the obtaining of SPM images undistorted by drift. Relief elements, such as a "hill" or "pit," are taken as features in the used recognition procedure. Since surface features are defined in the most general form, it is possible to detect an appropriate feature in the image in most of practical cases.

Positions of the same features in the CSIs do not coincide due to drift-induced distortions, and the degree of noncoincidence increases as receding from the CP. Numbers of features in CSIs are also different. Moreover, scanning failures result in the fact that some features recognized in one image can be unrecognized in another. Thus, after recognition of the features in the CSIs, the next iterative process is necessary, during which it is determined that a feature with the coordinates (x_1, y_1) in image 1 and a feature with the coordinates (x_2, y_2) in image 2 are the same feature with the coordinates $(\bar{x}, \bar{y})$ in the corrected image.

The iterative process begins at the CP and then propagates along the scanning path of the counter image. During the iterative process, pair features are detected exclusively by their closeness in position in the intermediate image corrected using intermediate LTCs.

The largest effect of the application of the described method of drift correction is achieved in feature-oriented scanning (FOS) [8], since this method allows drift correction in images of any size. The point is that the basic assumption about an unchanged drift velocity for the scanning time is necessarily violated beginning from a certain scan size. Although much the same assumption should be valid for scans obtained using FOS, the arising contradiction is resolved there, since the large area is scanned in parts, i.e., by small segments (square vicinities of surface features), and all movements are done for short distances from one feature to a nearby other feature.

When going from the atomic scale to surfaces with characteristic sizes of features and distances between them of tens and hundreds of nanometers, the external appearance of the drift thermal component in the image

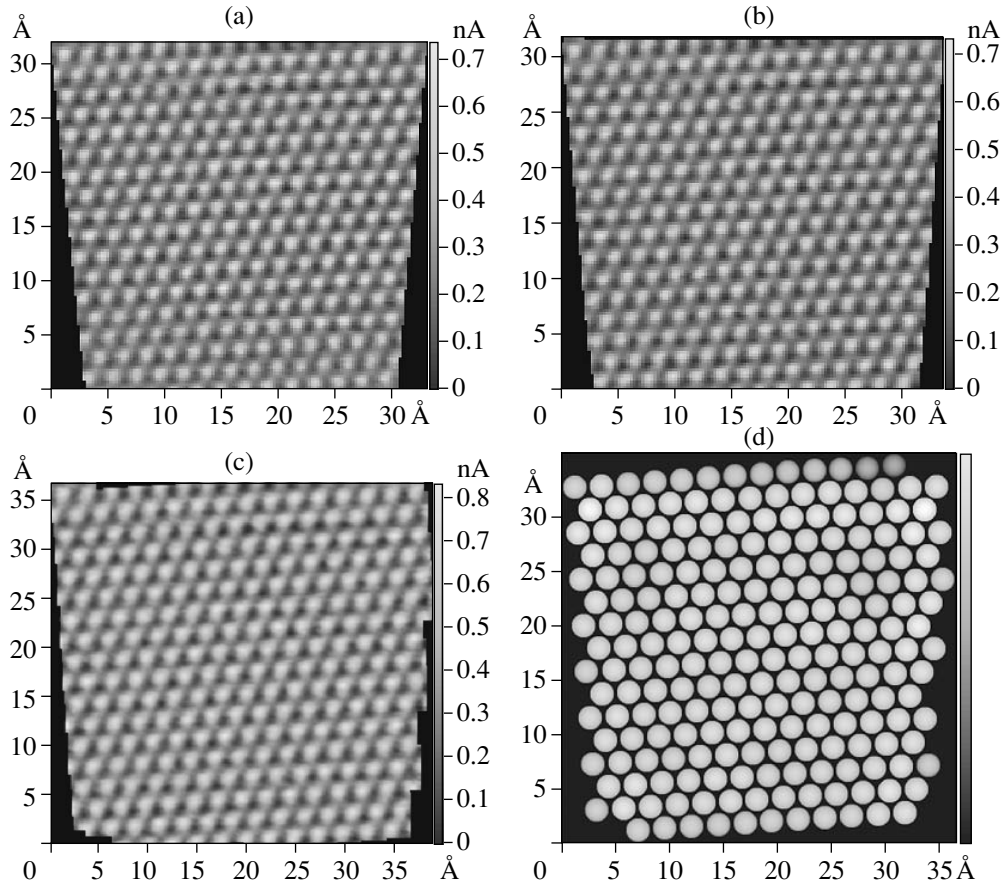

Fig. 2. Corrected atomic surface relief of pyrolytic graphite: (a) the linear correction, the average error over the image field is 0.3%; (b) the nonlinear correction performed using regression surfaces, the average error over the image field is 0.09%; and (c) the nonlinear correction using relief assembling from separate partially overlapping surface segments. The averaged lattice constant is 2.4638 Å, which corresponds to the relative measurement error of 0.01%. (d) The spherical model of the surface in panel (c).

weakens, whereas the external appearance of the nonlinear component from the creep is enhanced. Despite this fact, the adverse effect of creep can be significantly weakened by measuring the relief by parts in small segments and applying mutually counter motions of the probe in apertures, in segments, between neighboring features (skipping), and in feature lines which form a whole hierarchy of counter motions [8].

Moreover, in the case of an appreciable change in the drift velocity (continuously monitored in FOS), the measurement process is automatically terminated, the corrupted local data are rejected, and the microscope waits for drift velocity stabilization, periodically attaching the probe to a current surface feature or introducing idle skipping cycles. As soon as the drift velocity is stabilized, the operation is resumed by newly performing a terminated rejected local measurement. Thus, the above set of procedures results in the total drift again becoming a slowly varying process; hence, it is also linearizable.

Attention should be paid to the simplicity of the detection of the same feature in the CSIs when using FOS. The point is that the segment, as a rule, contains only one feature. When the segment contains several features (usually two or three), features located closer than others to CSI centers will correspond to the same current feature in the corrected segment, since the main attribute of the current feature in the segment is its closeness to the square raster center [8].

It should be noted that the number of image averagings is limited and cannot be more than four in the case of direct application of the described drift correction technique; on the contrary, there are no limitations on the number of averagings of images (segments) for application in FOS.

For surface scans characterized by a large number of features rather uniformly distributed over the image area, the following nonlinear correction method can be proposed. First, pairs of CSI features are determined using the above linear approach; then, local LTCs K_x and K_y are calculated for each pair. This yields a distribution in which proper lateral LTCs $K_x(x, y)$ and $K_y(x, y)$ are attributed to each feature with the coordinates x, y.

Using transformations (1), the local displacements $D_x(x, y) = \bar{x}(x, y) - x$ and $D_y(x, y) = \bar{y}(x, y) - y$ in the lateral plane are determined for each image feature with the real coordinates x, y. The displacements corre-

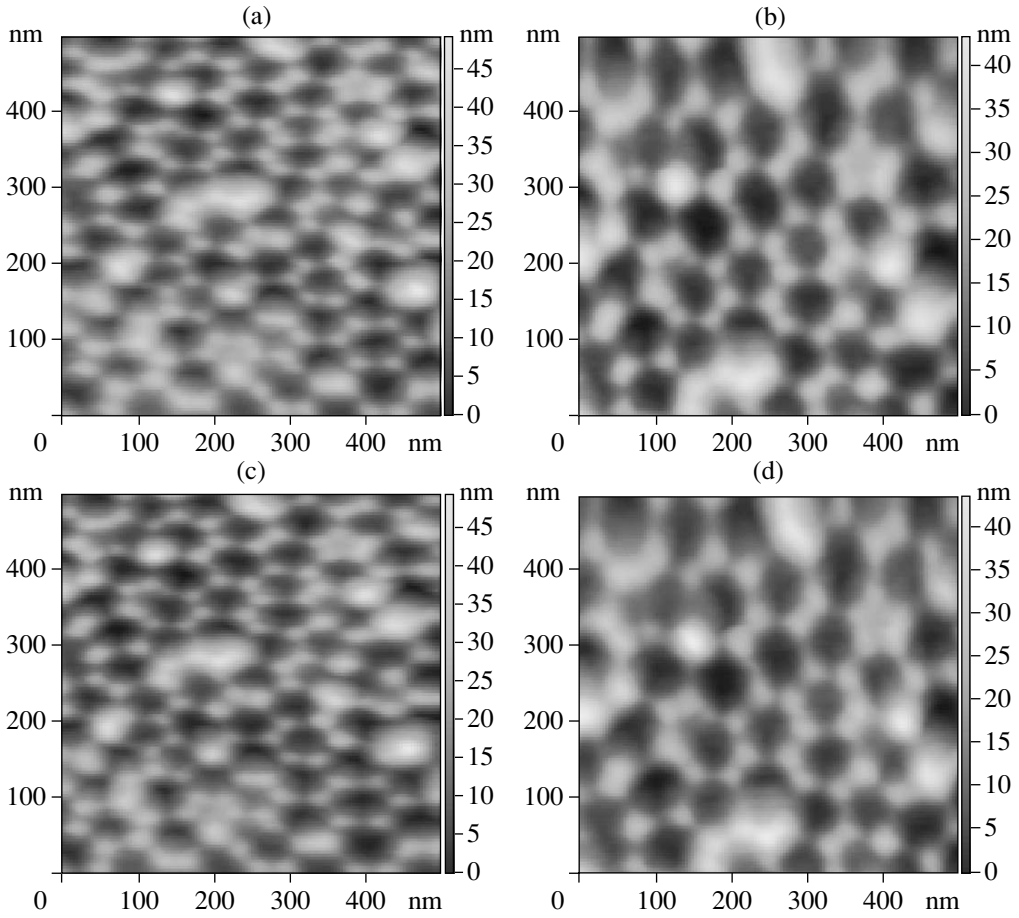

Fig. 3. Drift-distorted CSIs of the quasi-ordered porous alumina surface: (a, b) the first CSI pair and (c, d) the second CSI pair. Measurement mode: AFM; tapping; the cantilever force constant is ≈12 N/m; the resonance frequency is 290.295 kHz. The number of raster points is $m_x = m_y = 127$. The scanning step is $\Delta_x = 3.913$ nm, $\Delta_y = 3.935$ nm. The number of averagings at the raster point is 5. The scanning speed is $v_x = 1109.7$ nm/s ($k = 1$). The scanning time is 3 min 50 s. The average drift velocities in the lateral and vertical planes are 16.9 and 3.3 Å/s, respectively. The maximum drift-induced relative errors of measurements in the lateral plane are (a, b) 24.6% and (c, d) 24.4%.

sponding to the integer coordinates of distorted image points are determined by constructing regression surfaces through the obtained displacements. Finally, the image corrected in the lateral plane is obtained by applying local displacements to the corresponding points of the distorted SPM image.

To correct the drift in the vertical plane, the CSIs corrected in the lateral plane should be brought into coincidence by making coincident the centroids of the feature sets used. By calculating the local coefficient K_z and then the difference between the corrected relief height and that distorted at each point $(\bar{x}, \bar{y})$ of the CSI overlap area, we determine the distribution of local displacements over the image field in the vertical plane, $D_z(\bar{x}, \bar{y}) = \bar{z}(\bar{x}, \bar{y}) - z(\bar{x}, \bar{y})$. The working distribution is determined to perform nonlinear correction of the image in the vertical plane by constructing the regression surface through the found local displacements.

Another nonlinear correction scheme is as follows. A certain square vicinity (a segment) is cut around a feature in each corrected image; then the cut relief fragments are placed in a position being an average of corrected positions of this feature in the corresponding CSI. The images and the feature positions can be corrected by both the linear and nonlinear methods described above. The relief is averaged in the places of overlapping segments.

The described nonlinear correction methods are validated by the fact that the actual feature position is somewhere in the segment between the corrected feature positions and is most likely attracted to the center.

EXPERIMENTAL RESULTS

To verify the validity of the proposed method, a small area of an ordered surface of highly oriented pyrolytic graphite was counter-scanned. The relief was scanned using a Solver™ P4 microscope (produced by the NT–MDT Co., Russia) in the constant-height mode in air after many hours of instrument warming. As a result, two CSI pairs were obtained (Fig. 1).

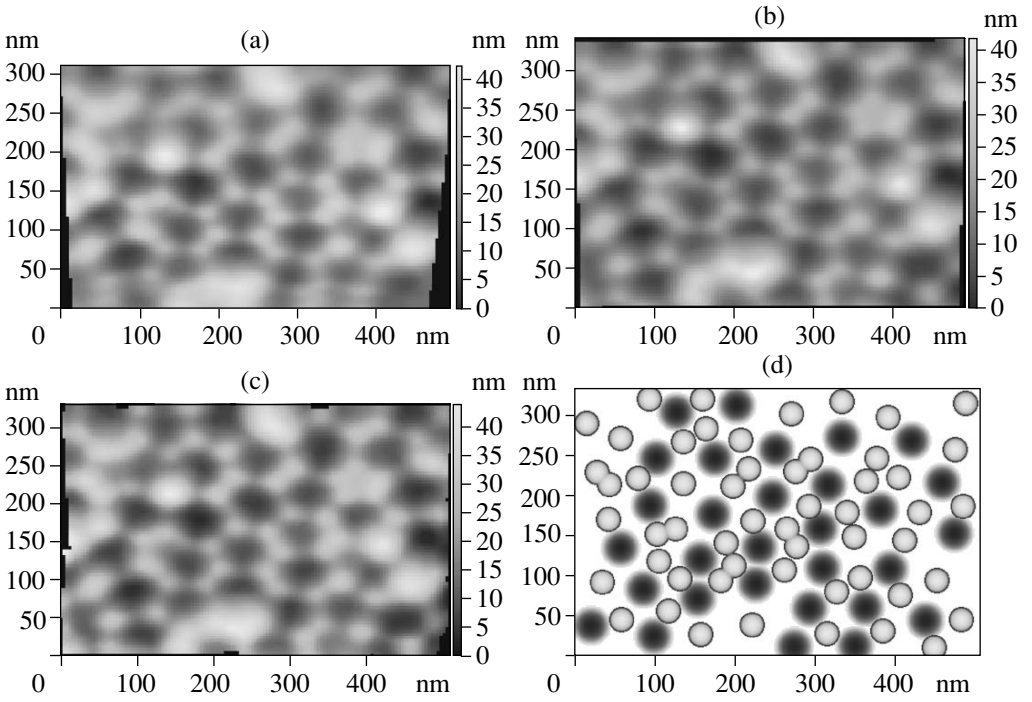

Fig. 4. Corrected relief of the porous alumina surface: (a) the linear correction, the average error over the image field is 1.5%; (b) the nonlinear correction using regression surfaces, the average error over the image field is 0.16%; (c) the nonlinear correction using relief assembling from separate partially overlapping surface segments, the average distance between pores is 69.9 nm; and (d) the stylized image.

Drift-induced distortions of the atomic relief are clearly seen in the figures presented in this paper. Figure 2 shows the current relief of the graphite surface, which is corrected by a linear and two nonlinear correction methods; a stylized image of the graphite surface is also shown.

The images in Figs. 2a and 2b still contain systematic errors of microscope scanner calibration (~14%) performed earlier disregarding drift-induced distortions. Using the automatic calibration technique described in [11], the correction coefficients $\overline{K}_x$ = 1.1896, $\overline{K}_y$ = 1.1429 and the nonorthogonality angle $\alpha = 0.4°$ between *X*- and *Y*-piezoelectric manipulators were determined. In Figs. 2c and 2d, the indicated scaling errors are eliminated. The averaged lattice constant in these images is 2.4638 Å (the nominal value is 2.464 Å), which corresponds to a relative measurement error of ~0.01%.

Figure 3 shows the CSIs of a quasi-ordered porous alumina surface. Alumina pores were produced by aluminum foil anodizing in an aqueous solution of oxalic acid [12]. To better view the morphology details, the average surface slopes were preliminary subtracted from these images. In the absence of defects, each pore is surrounded by six neighboring pores forming a regular hexagon. Six small hillocks are arranged around the perimeter of each pore hole, which also form a regular hexagon.

During the experiments in ambient air, it was noticed that the porous alumina surface adsorbs well atmospheric moisture; i.e., it is hydrophilic. The surface water layer makes pore resolution practically impossible. An attempt to pierce this layer by increasing the pressing force of the cantilever probe (the cantilever from NT–MDT was used in the experiments) and to measure the solid relief did not yield good results. It also failed to obtain a distinct signal after increasing the amplitude of free oscillations of the cantilever.

It became possible to see pores themselves and the finer structure, i.e., a fringe of six hillocks, only after removal of the adsorbed water layer by heating the sample at a temperature of 70–80°C for a few minutes. The surface "lifetime" after turning off the heater is 10–15 min at room temperature and a relative humidity of 50–70%, after which the surface is again "overgrown" and becomes inapplicable for high-resolution scanning. It was also detected that the scanning process stimulates moisture redistribution/adsorption on the porous surface, because repeated scanning of already scanned areas yielded worse contrast in comparison with the neighboring areas where scanning was later carried out for the first time.

Since the microscope had no heater built into the sample holder, heating was performed outside the microscope. The hot sample was placed in the microscope and scanned for 5–10 min. Because of the above time limitations, counter-scanning was performed

almost immediately after the probe approach and detection of a suitable porous surface area.

Thus, due to the impossibility of long relaxation of the microscope, in addition to the creep arising during scanning and the thermal drift typical of the microscope, the following additional drifts occurred during measurements of the alumina topography: the *Z*-manipulator creep after approach, the *X*- and *Y*-manipulator creeps resulting from the probe offset to the position of scan origin, and the thermal drift fraction formed under nonuniform cooling of the holder and sample after their heating to the above-mentioned temperature. Solidification of double-sided adhesive tape used to fix the sample probably also caused an additional motion.

The total effect of the above adverse factors distorts the image so strongly that the counter scan contains only half of the surface area obtained by forward scan. Despite such significant distortions, even the linear model allows correction of such images with a quite acceptable error (Fig. 4a). Figures 4b and 4c show the porous alumina relief corrected by nonlinear methods; Fig. 4d shows its stylized image.

The materials presented in this paper were reported at the International Symposium "Nanophysics and Nanoelectronics," Nizhni Novgorod, Russia, March 25–29, 2005.

ACKNOWLEDGMENTS

The author is grateful to S.Yu. Vasiliev for critical remarks on the manuscript, S.A. Saunin for his assistance in embedding the counter-scanning into the SPM control program, and S.A. Gavrilov for the porous alumina sample.

This study was supported by the Russian Foundation for Basic Research (projects nos. 05-01-00407, 05-03-32394, and 08-07-00003) and the Government of Moscow (project no. 1.1.213).

REFERENCES

1. J. E. Griffith and D. A. Grigg, J. Appl. Phys. **74**, R83 (1993).
2. J. E. Griffith, G. L. Miller, C. A. Green, et al., J. Vac. Sci. Technol. B **8**, 2023 (1990).
3. V. B. Elings, J. A. Gurley, and M. R. Rodgers, US Patent No. 5,077,473 (1991).
4. R. Robinson, US Patent No. 5,107,113 (1992).
5. V. Y. Yurov and A. N. Klimov, Rev. Sci. Instrum. **65**, 1551 (1994).
6. J. F. Jørgensen, L. L. Madsen, J. Garnaes, et al., J. Vac. Sci. Technol. B **12**, 1698 (1994).
7. R. V. Lapshin, RU Patent Appl. No. 2 006 127 131 (2006); www.nanoworld.org/homepages/lapshin/patents.htm.
8. R. V. Lapshin, Nanotechnology **15**, 1135 (2004); www.nanoworld.org/homepages/lapshin/publications.htm.
9. E. P. Stoll, Rev. Sci. Instrum. **65**, 2864 (1994).
10. R. V. Lapshin, Rev. Sci. Instrum. **66**, 4718 (1995); www.nanoworld.org/homepages/lapshin/publications.htm.
11. R. V. Lapshin, Rev. Sci. Instrum. **69**, 3268 (1998); www.nanoworld.org/homepages/lapshin/publications.htm.
12. A. P. Li, F. Müller, A. Birner, et al., J. Appl. Phys. **84**, 6023 (1998).